Hierarchically Built Hetero-superstructure Arrays with Structurally Controlled Material Compositions

Vignesh Suresh,[†] Srinivasan Madapusi,[†] and Sivashankar Krishnamoorthy[‡,§,*]

[†]Department of Chemical and Biomolecular Engineering, National University of Singapore, Blk E5, 4 Engineering Drive 4, 117576, Singapore, [‡]Institute of Materials Research and Engineering (IMRE), Agency for Science, Technology and Research (A*STAR), 3 Research Link, 117602, Singapore, and [§]Science et Analysis des Materiaux (SAM), Centre de Recherche Public-Gabriel Lippmann, 41 Rue du Brill, Belvaux, 4422, Luxembourg

ABSTRACT Hierarchical assemblies are repeatedly encountered in nature, and when replicated in synthetic patterns and materials, can enhance their functionality or impart multifunctionality. In order to assemble a hierarchical superstructure that consists of components made up of multiple nanostructures, control over placement and stoichiometry is desirable. Macroscopic arrays that present up to three levels of hierarchy are demonstrated here and are achieved using the self-assembly of soft, collapsible block copolymer nanospheres for the first two levels, followed by directed self-assembly of metal nanospheres for the third. The fabrication approach combines advantages of soft sphere self-assembly to yield non-close-packed and variable array pitch values, with the inherent chemical functionality presented by the polymer-based soft spheres; these assemblies can then be transformed into a range of different materials, including metal or semiconductor nanostructures, or further tailored with an additional level of complexity. Structural investigation shows the superstructure formation to be governed by generic design rules that can be extended across different material combinations.

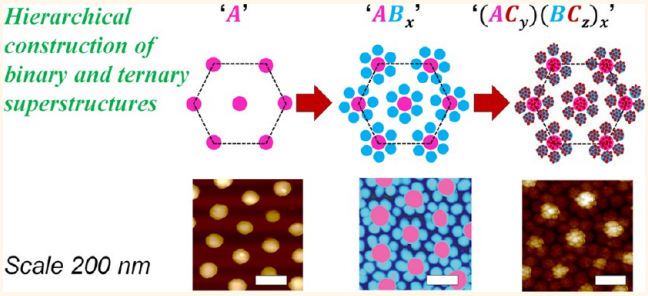

KEYWORDS: clusters · hierarchy · self-assembly · block copolymer · heterostructures · nanopattern · nanoparticle · nanostructure · superstructure

Hierarchical nanopatterns display attractive properties arising out of multiple length scale structuring and added functionalities. Lotus leaves,[1] butterfly wings,[2] moths' eyes,[3] and numerous other biological surfaces display special properties traceable to their hierarchically nanostructured surfaces. Hierarchy allows one to add multiple functionalities, one on top of another, thus enabling a precise control over the extent of functionality of each type. Ordered multilevel hierarchies have been realized through fabrication employing colloids,[4] supramolecules,[4,5] or lithography,[6,7] but those presenting beyond a second level of hierarchy in the submicrometer or nanoscale are rarely encountered. We demonstrate here an entirely self-assembly-driven approach to two-dimensional arrays of binary or ternary superstructures of *ABx* and (*ACy*)(*BCz*)*x* type, where $C \in B$, *A* and *A*, *B*, *C* are nanostructures with dimensions of <100 nm. Each level of hierarchy in the superstructure can be engineered to present a different material and its degrees of hierarchy (*x*, *y*, *z*) tuned to control its composition. The assemblies present a branched hierarchy in binary superstructures and a mixture of branched and nested hierarchies in ternary superstructures. The degree of branching (*x*) in binary assemblies is controlled by tuning the separation between features in the parent hierarchy (*A*) in relation to the size of branched component (*B*). The degree of nesting (*y*, *z*) in the ternary superstructures is determined by the size of the nested component (*C*) in relation to that of parent components, *A* and *B*, respectively. Generic design principles that we extracted from the investigation of these assemblies can be extended to design new multifunctional systems with tailored geometric attributes. Such entirely self-assembly-derived hybrid material hierarchies

* Address correspondence to sivashankar.krishnamoorthy@lippmann.lu.

Received for review February 25, 2013 and accepted August 4, 2013.

Published online August 04, 2013
10.1021/nn400963a

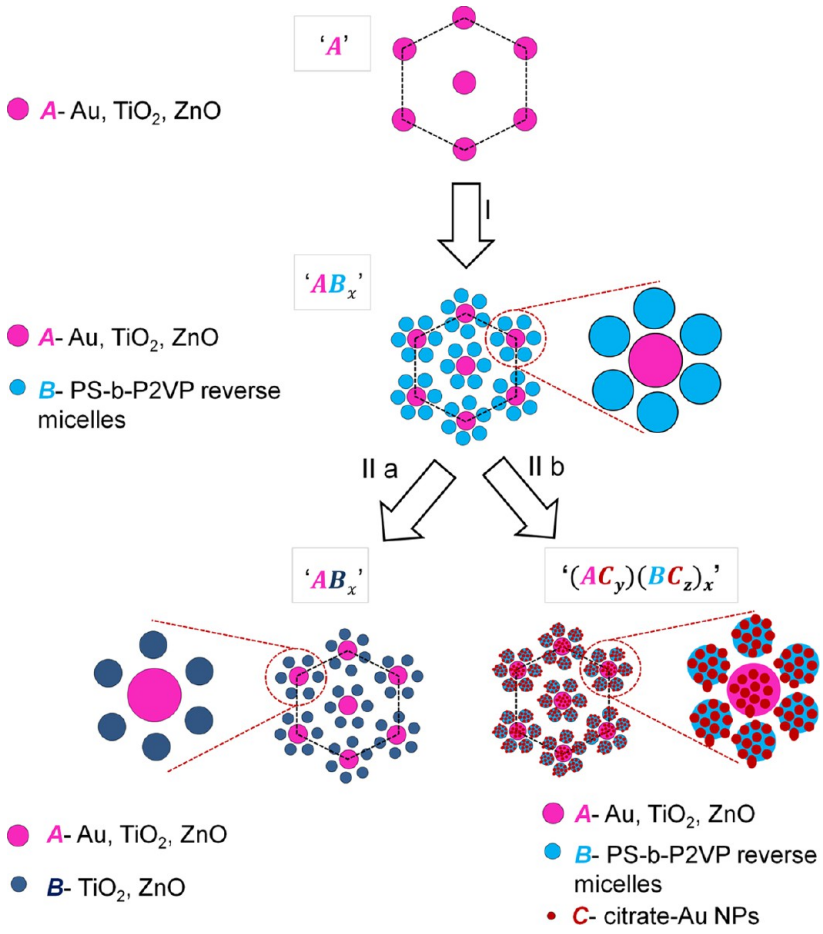

Figure 1. Schematic illustration of binary and ternary superstructures demonstrating the flexibility in the choice of material combinations realized in this work. Dotted lines are intended as visual guides. *x* denotes the number of *B* organized around each *A* feature; *y* and *z* denote the average number of *C* features organized onto each *A* and *B* feature, respectively.

with rich flexibility in the choice of material type and stoichiometries are unprecedented and have high implications for photonic, optoelectronic, and biodevice applications.[8−15]

By virtue of employing a combination of hard and soft spheres for assembly formation, our superstructures differ from 3D nanoparticle superlattices, *e.g.*, binary (BNSL)[16−20] and ternary superlattices (TNSL),[21,22] 2D lattices of submicrometer spheres,[23] or the confined organization of micro-[24,25] or nanospheres,[26−28] in the driving force behind the self-assembly of components and in the realizable configurations. These assemblies predominantly rely on the space-filling factors of close-packed spheres or directed assembly onto pre-existing lithographic templates as driving forces for assembly formation. Both these approaches are generic and successful in yielding hierarchical assemblies, except when encountered with strenuous demands of scalability and ease of controlling relative arrangements of nanoscale components. Hierarchical construction has also been carried out in the solution phase through preparation of nanoparticle clusters with a well-defined number of particles per cluster through careful engineering of the nanoparticle's surface using molecular linkers.[29−35] Such clusters are especially interesting in the context of optical phenomena arising from the close proximity between metal nanostructures.[30,31] The approach however is limited when larger clusters are desired or when the clusters have to be organized on the surface with well-defined feature separations and densities suitable for on-chip devices. In this direction, the generic approaches demonstrated in our work enable the realization of binary and ternary hetero-supercluster arrays with tailorable geometries and profound flexibility in the choice of material combinations. This is achieved through a hierarchical construction exploiting the capillary force driven assembly of soft, functional polymer spheres at the first two levels of hierarchy and directed electrostatic attachment of preformed nanoparticles at the third level (Figure 1). The use of non-close-packed and collapsible soft polymeric spheres at the first two levels is the key to attaining these superstructure arrays with high structural tunability and with easy scalability to arbitrarily large areas. The composite functionality of the polymeric spheres enables further independent ramifications in the attainable material nanostructures,

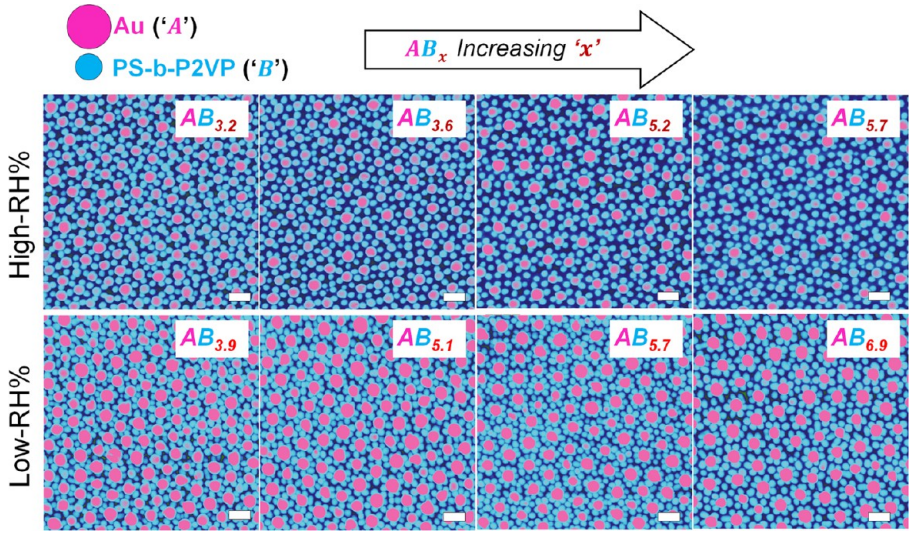

Figure 2. Tapping mode AFM images of binary superclusters of *ABx* type, with *A* corresponding to Au and *B* to PS-b-P2VP, prepared at high (55%) and low (<10%) relative humidity (RH%), with an increasing value of *x* from left to right. Scale bar indicates 200 nm. The images are shown in false color, with *z*-scale chosen to provide adequate lateral contrast. The pink pixels represent greater topography than blue pixels (refer to Figure S1 in the SI for *z*-scale information).

thereby allowing realization of superstructures with a range of material combinations.

The first level or the highest ranking hierarchy (*A*) consists of an inorganic metal or semiconductor nanoparticle array achieved by *in situ* synthesis within self-organized copolymer reverse micelles on the surface.[36,37] The reverse micelles are soft nanospheres that form non-close-packed arrays on the surface with opportunities for systematically variable pitch, simply by varying spin-coating speeds.[37,38] The second level is attained by exploiting features in the first level as nodes to drive self-organization of diblock copolymer reverse micelles (*B*) of smaller dimensions through capillary forces. The separation between *A* features is on the order of the size of *B* and thus provides a confining influence and determines the number of *B* features organized around each *A*. The ratio (δ) of separation (s_A) between *A* features to the diameter (d_B) of *B* allows fine control over the degree of branching *x*, and it also governs the transition from branching to overlapping hierarchies in the resulting *ABx* superstructures. The composite functionality of *B* permits its further independent translation into other metal or semiconductor materials of interest (Figure 1, step IIA) or toward adding a third level of hierarchy (Figure 1, step IIB). The third level of hierarchy is attained through the attachment of smaller nanoparticles to the surface of *A* and *B* through electrostatic interactions. This results in a nested hierarchy with a degree of nesting, *y* or *z*, in $(AC_y)(BC_z)_x$ determined by the surface area of *A* or *B* in relation to the size of *C*.

RESULTS AND DISCUSSION

Fabrication of *ABx* Superstructures with *x* Determined by Edge Separations in *A* Arrays. Binary superstructures of *ABx* type, with *A* corresponding to *Au* and *B* corresponding to PS-*b*-P2VP reverse micelles, with systematic variation in *x* are shown in Figure 2. The fabrication of the *Au*(*PS-b-P2VP*)*x* superstructures starts with the preparation of Au nanoarrays that constitute the first level of hierarchy. The Au arrays are realized by *in-situ* synthesis[39] within the P2VP core of self-organized PS-*b*-P2VP (380 kDa, $f_{PS} \sim 0.5$) reverse micelle arrays, in two consequent steps: the micelle array coated chip is immersed into an aqueous solution of $HAuCl_4$ to enable loading the gold salt within the core of PS-*b*-P2VP reverse micelles; the polymer template is subsequently removed by subjecting the salt-loaded reverse micelles to oxygen plasma exposure (see methods for experimental details). This results in Au nanoarrays with periodic arrangement of Au nanoparticles, exhibiting feature heights of 50 ± 5 nm. The centre-to-centre distance (periodicity) of the array can be systematically varied between 150−225 nm by varying the spin-coating speeds employed for deposition of PS-*b*-P2VP reverse micelles on surface. Spin speeds of 1000, 2000, 4000, and 6000 rpm result in periodicity of 154, 167, 200, and 222 nm, respectively. The fine tunability in periodicity of the reverse micelle arrays translates into an ability to fine-tune edge-to-edge separations between the Au features (s_A) to 85, 103, 134, and 144 nm, respectively.[26,38] The second level hierarchy consists of reverse micelles of PS-*b*-P2VP (114 kDa, $f_{PS} \approx 0.5$) coated onto pre-existing Au particle arrays. The reverse micelles used in this step are of a smaller size in relation to those used to generate the first level of hierarchy (refer to Figure S2 for dynamic light scattering measurements). These micelles organize themselves along the periphery of the Au nanoparticle features

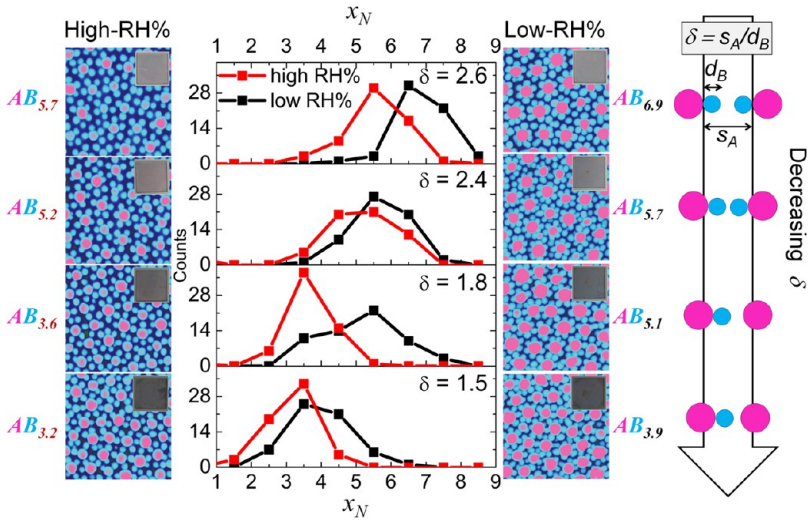

Figure 3. Binary superstructures of *ABx* type, with *x* determined by the ratio (δ) of separation between *A* features (s_A) to the diameter of *B* features (d_B). The histogram of the number of *B* (reverse micelles) present around each *A* (Au nanoparticle) shows systematic control in *x* with variation in δ. Insets show pictures of corresponding Si chips (1 cm × 1 cm), with *ABx* superstructure arrays uniformly spanning the entire area.

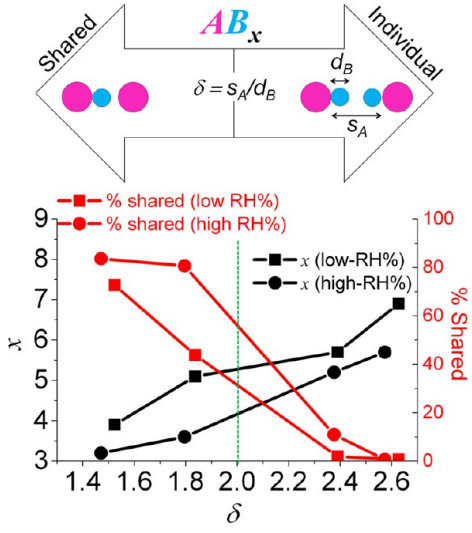

Figure 4. Dependence of *x* and '% shared' on δ and the formation of branching and overlapping hierarchy above and below δ = 2, respectively.

by capillary forces, yielding well-defined binary superstructures with degree of hierarchy (*x*) determined by the ratio (δ) of the separation (s_A) between *Au* features (*A*) to the diameter (d_B) of reverse micelle features (*B*) (Figure 3). The degree of hierarchy (*x*) is defined by the peak value of Gaussian fit to the histogram of x_N. x_N is defined as the number for *B* features present around the *A* feature in the N^{th} superstructure. The histogram of x_N is generated from a tabulation of the number of *B* features in each superstructure from AFM images of the *ABx* arrays shown in Figure 2. The systematic variation in *x* as a function of δ can be seen as a progressive shift in the mean value of the histograms as shown in Figure 3. As s_A decreases, there is an increasing overlap between adjacent superstructures, thereby resulting in an overlapping hierarchy (Figure 4). The value of x_N in case of overlapping superstructures was obtained by counting the number of *B* features weighted by their occupancy in the superstructure (equation a). Each *B* feature surrounding the *A* features is assigned an occupancy of 1, (1/2) or (1/3) depending on whether it remains unshared, or if it is shared by 2 or 3 adjacent *A* features, respectively. This avoids double counting of the features and presents the real scenario of the density in *B* features in relation to that of *A*. The value of *x* systematically decreases with an increase in overlap between the adjacent superstructures. In the dependence of *x* on δ, the branching hierarchy is observed for values of $\delta > 2$ and overlapping hierarchy for values below. This is expected, as illustrated in Figure 4, since $\delta = 2$ represents a value for separation between the *A* features that is twice the diameter of *B*, and thus for $\delta < 2$ there is insufficient space to support independent superstructures. Even at the lowest feature separations, the maximum sharing is observed to be only 80% (as estimated by equation b) due to the presence of some *B* features that remain unshared. The presence of unshared *B* features is a consequence of greater distance between some *A* features compared to others as a result of standard deviation in separations. The influence of standard deviation is also seen in the case of branching hierarchies ($\delta > 2$) to result in few isolated *B* features occupying the space between superstructures.

$$x_N = \sum_{i=1,\,1/2,\,1/3} (n_i \times i) \text{ where,}$$

$$i = \frac{1}{\text{Number of } A \text{ features that share the } B \text{ feature}},$$

and n_i indicates the number of *B* features with an occupancy of *i*

(a)

$$\% \text{ shared} = \frac{\text{Occupancy of shared features}}{\text{Total occupancy per superstructure}} \times 100$$

$$= \left(\frac{\sum_{i=1/2,\,1/3} (n_i \times i)}{\sum_{i=1,\,1/2,\,1/3} (n_i \times i)} \right) \times 100 \qquad \text{(b)}$$

Influence of Relative Humidity on the Composition of Binary Superstructures. In addition to the influence of δ on x, there is an additional influence noticed due to the relative humidity of the medium. The values of x were higher when the reverse micelles (B) were coated on to the Au nanoarrays at a relative humidity (RH%) of <10% as compared to the ambient value of 55%. It is important to note that the influence due to relative humidity is felt only at the time of the film formation, since a postexposure of the coatings has no effect on the resulting assemblies. The influence is difficult to predict given that the coatings are deposited from an apolar medium, and thus, the presence of moisture in the environment is not expected to influence the evaporation rate, as it would for aqueous counterparts. There are, however, other ways in which the humidity can indirectly influence the quantity of material deposited on the surface, which is through a significant increase in adlayers of water on the surface with an increase in relative humidity.[40−44] Such adlayers can potentially decrease wettability of the surface toward apolar solutions, causing an increase in outflow rates during spin-coating and resulting in a lower film thickness at high relative humidity.[45] This premise agrees with the correlation between film thickness and surface wettability observed in literature, for polystyrene thin films spin-coated from toluene solutions onto topographically patterned substrates.[46] Other related instances of the influence of humidity reported in the literature include, increase in volume of meniscus formed at the interface of a nanoscale probe and surface by capillary condensation[47] increase in transport rates for apolar inks in dip-pen lithography,[47] and drastic decrease in the nanoscopic sliding friction experienced by the tip on rough and hydrophilic surfaces.[44,48]

To gain better insight into the potential influence of relative humidity on the outflow rates during spin-coating, a control experiment was set up to determine sliding contact angles of a mineral oil on the substrates consisting of the Au nanoparticle arrays (the first level of hierarchy, or the A features as in Figure 1). The sliding angles reflect the adhesive forces between the droplet and the surface, which in turn has an indirect influence over the outflow rates during spin-coating. A mineral oil (Vaccubrand B-oil) with low vapor pressure was chosen for the experiment to ensure no evolution in droplet size occurred during the measurements. The surface tension of the oil (31.2 ± 0.03 mN/m), measured using the Wilhelmy ring method, is close to that of m-xylene (28.9 mN/m),[49] thus allowing an extrapolation of its behavior to that of m-xylene solutions of reverse micelles. A tiny quantity of the mineral oil (~15 μL) was pipetted on a horizontally placed chip, and the chip slowly tilted (custom-designed setup) until the oil rolled off. A sliding angle of 22.9 (±2°) was observed at high RH% (~55%) and 30.2 (±2°) for low RH% (<10%) environments, ascertaining a greater ease of roll-off for the oil droplet at higher humidity. This was found to be also true for bare Si chips, yielding 24.1 (±2°) and 29.0 (±2°) at high and low RH%, respectively, although with a slightly lower contrast between the roll-off angles as compared to the case of Au nanoparticle arrays. The greater ease of roll-off of the oil droplet at a high RH% environment shows a lower adhesion and supports arguments that water adlayers acting as a lubricating layer facilitates greater outflow of the apolar reverse micelle solution during spin-coating. Additional control experiments were run to ascertain the densities of PS-*b*-P2VP reverse micelles (0.5% w/w in m-xylene spin-coated at 3000 rpm, the same as employed for *ABx* superstructure experiments) on bare Si substrates, at high and low RH%. The arrays coated at RH < 10% show a greater quantity of deposition (refer to Figure S3 in the SI for AFM images), as manifested through a higher value for the density (154 ± 9/μm^2) of the micelles as compared to coatings done at high RH% (113 ± 6/μm^2). We say "quantity" rather than "thickness" because, in the case of reverse micelles, within the window of conditions we operate (for solution concentrations of 0.5−1.0% w/w and spin-coating speeds of 1000−6000 rpm) an increase in polymer quantity on the surface is manifested as an increase in density of features rather than an increase in film thickness. Thus, our observation of the influence of humidity on the thickness of the spin-coated film is generic and not specific to reverse micelles used in the study. The control over humidity allows the process to fine-tune as well as maximize values for x in the binary hierarchies.

Influence of Feature Size of *A* over *x* in *ABx* Superstructures. Besides the dependence of x on δ, it is interesting to extend the understanding further to decipher its dependence on the feature size of A in relation to that of B. The AFM measurements show a standard deviation of 10% in the size of A features, which in turn contributes to a standard deviation in the degree of branching of B features in the resulting *ABx* superstructures (Figure 3 histograms). Thus, by tabulating the degree of branching (x_N) against the ratio of diameters of B to A (d_B/D_A) for each of the individual superstructures appearing in the AFM image of an nonoverlapping *ABx* hierarchy (*e.g.*, $AB_{5.7}$ or $AB_{6.9}$), the dependence of x_N *versus* d_B/D_A can be deduced. The comparison of x_N *versus* d_B/D_A (shown for $AB_{6.9}$ superstructures in Figure 5) shows a systematic

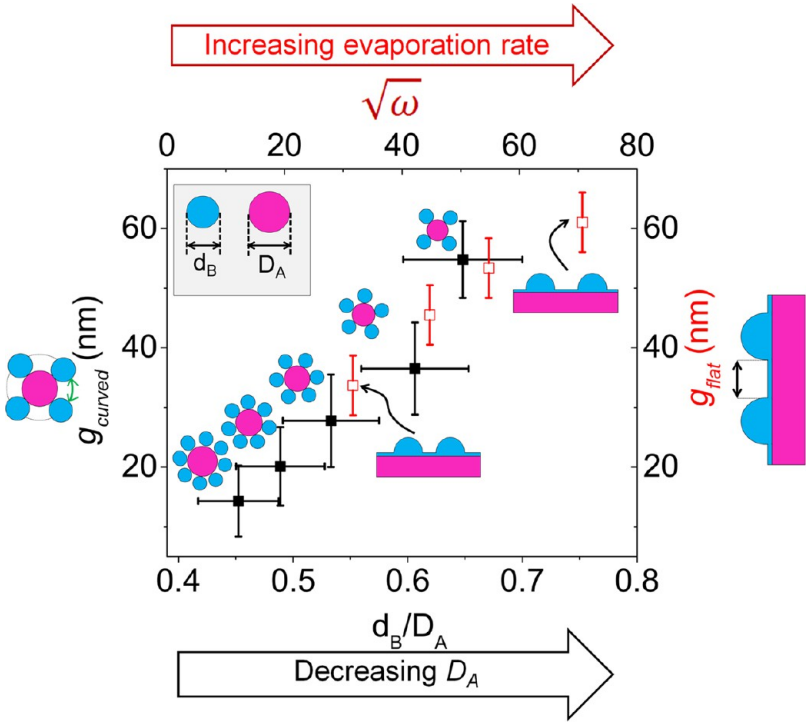

Figure 5. Systematic increase in g_{curved} with d_B/D_A ratio for $3 < x_N < 8$ in $AB_{6.9}$ superstructures is found to match the trend of increase in g_{flat} with an increase in the evaporation rate (represented as $\sqrt{\omega}$, where ω represents spin-coating speeds in rpm) on flat substrates. The *x*-axis errors shown for d_B/D_A include the contribution due to the coexistence of D_A values per x_N.

increase of x_N with D_A, which is expected, based on the increasing peripheral space around the *A* features. However, a rather subtle and unexpected influence of D_A is noticed on the density of micelles (or how closely the micelles are packed) within the superstructure. This influence is best demonstrated through an estimation of feature separations (g_{curved}) of micelles within each superstructure using values for D_A, d_B, and x_N obtained from AFM in the equation c (derived from simple geometric considerations, as shown in Figure S4, in the SI). d_B is taken as a constant, with a value of 55 nm.

$$g_{curved} = \frac{\pi(D_A + d_B) - x_N d_B}{x_N} \qquad \text{(c)}$$

A systematic increase in g_{curved} with d_B/D_A ratio for $AB_{6.9}$ superstructures of $3 < x_N < 8$ is shown in Figure 5. The plot of x_N *versus* D_A reveals that a specific value of x_N is exhibited by a range of D_A values (refer to Figure S5 in the SI for a plot of x_N *versus* D_A/d_B). The *x*-error bars in Figure 5 take this coexistence into account; in addition, they include errors due to tip convolution effects in the determination of D_A and d_B. Although these error bars seem large (mainly due to coexistent D_A values per x_N), the trends noticed in the decrease in g_{curved} with an increase in D_A or decrease in d_B/D_A ratios are unmistakable. One way to account for this trend is by considering a greater meniscus volume of the polymer solution associated with larger sized *A* features, which as a consequence results in a higher density of micelles at its periphery. However, our estimation of the equivalent volumes of the polymer solution that would carry as many micelles as x_N reveals ~164−437 attoliters for x_N values of 3−8 (an explanation of the estimation is provided in the Methods section). These volumes are 3 orders of magnitude higher in comparison to those of the *A* features (estimated to be 0.09−0.48 attoliters for *A* features with D_A in the range of 68−122 nm considered in Figure 5) and equates to solution films that are much thicker than the *A* features. Thus, we rule out meniscus volumes around the template as a contributor to the observed dependence of x_N on the d_B/D_A ratios. The onset of meniscus contribution is expected when the thickness of the drying film approaches the height of *A* features.[50] However, by then, the x_N values have already been decided by the system, thus requiring an alternative explanation to the above dependence. We expect this dependence to arise because of a higher rate of evaporation on smaller *A* features due to their larger surface to volume ratio. The range of D_A values in Figure 5 represents an enhancement in surface to volume ratio of ~79% going from the largest to the smallest particles. During the evaporation of the solvent, the meniscus forces drive the micelles from both above and surrounding the *A* features to its periphery (Figure S6 in the SI for schematic illustration). The periphery of larger features would experience a relatively higher inflow of reverse micelles due to longer residence durations of the polymer

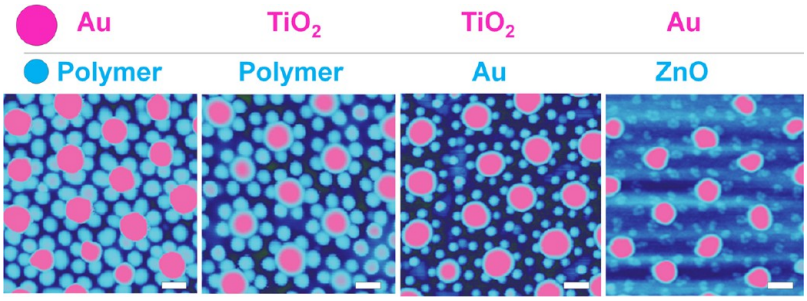

Figure 6. Arrays of hetero-superstructures of *ABx* type across a rich variety of *A*- or *B*-type materials can be readily achieved. From left to right are *Au*(PS-*b*-P2VP)$_x$, *TiO*$_2$(PS-*b*-P2VP)$_x$, *TiO*$_2$(*Au*)$_x$, and *Au*(*ZnO*)$_x$, respectively. Scale bars are 100 nm. Refer to Figure S7 in the SI for measurements across 2 μm $\times$ 2 μm and *z*-scale information.

solution resulting from a lower evaporation rate. Such influence of the evaporation rate on the density of micelles is known for coatings obtained on flat substrates,[38] where micelle arrays formed at higher spin speeds (higher evaporation rates) result in lower feature densities. The data obtained from flat chips is overlaid in Figure 5, with the evaporation rate represented as a square root of spin-coating speeds ($\sqrt{\omega}$) as known from the theoretical treatment of the spin-coating process.[51,52] The similarity in trends for g_{curved} *versus* d_B/D_A to g_{flat} *versus* $\sqrt{\omega}$ strongly favors attributing the former dependence to the size-dependent evaporation rate on *A* features. Establishing clarity on this influence allows the formulation of rational design rules to tailor-make superstructures with desired g_{curved}, d_B, and D_A even if the *A* features were to be fabricated by other means, *e.g.*, nanoimprint lithography or e-beam lithography.

The results establish separations between features in the first level as a convenient handle to tune the stoichiometries of the superstructures and to draw insights on the influence of the density of *B* features on the size of *A* and influence due to relative humidity. The ability to extend the understanding drawn from these results to realize *ABx* arrays of different material types is presented in Figure 6. The results convincingly support the versatility of the approach in yielding patterns of desired material combinations with stoichiometries that can be predicted beforehand. Since both the first and the second levels of hierarchy employ reverse micelles, the attainable combinations for *A* and *B* are fairly large, since solution-phase as well as vapor-phase precursors can be used to synthesize materials within the functional core of the reverse micelles.

Fabrication of Ternary Superstructures. The ternary superstructures of type (*ACy*)(*BCz*)*x* (Figure 7) were realized upon immersion of the binary superstructures of *ABx* into an aqueous suspension of citrate-stabilized Au nanoparticles (*C*) of ~11.7 nm diameter (refer to Figure S8 in the SI for TEM of Au nanoparticles employed). Since the *B* features constitute PS-*b*-P2VP reverse micelles, the citrate-stabilized Au nanoparticles attach themselves selectively to the surface of the *B* features due to electrostatic attraction and form Au nanoparticle clusters (*BCz* type).[26] The size of these clusters (as defined by the number of nanoparticles adhering to each micelle) is determined by the surface area of the template feature, which we demonstrated in our earlier study to be ~18 particles/cluster (thus, $z \approx 18$).[26] In the present case, the citrate-Au nanoparticles were found to attach not only on the micelles but also onto the central Au nanoparticle (*A* features). The latter is unexpected and is likely a consequence of the presence of a thin PS-*b*-P2VP layer[53] formed instantaneously on the surface of the *A* features, during the coating of the reverse micelle solution. When present, the PS-*b*-P2VP molecules would render the *A* features positively charged at the pH of 6.5 (corresponding to the citrate-Au nanoparticle suspension) and consequently direct attachment of negatively charged citrate-Au nanoparticles from the solution in a manner similar to that of the reverse micelles. The number of citrate-Au nanoparticles adhering to the *A* features can be estimated[26] based on the surface area of the *A* features to be 67 particles. However, the number of citrate-Au nanoparticles was observed to be far less in comparison, ~17 $\pm$ 4 particle per *A* feature (thus, $y \approx 17$) based on SEM measurements at high magnification. The significant drop in density of citrate-Au nanoparticles is likely due to the lower electrostatic attraction on the *A* features, presumably due to the low density of PS-*b*-PVP molecules on its surface. An additional contribution is likely due to the electrostatic repulsive forces from the citrate-Au nanoparticles on the neighboring micelle features, thereby excluding adsorption on the periphery of *A* features. Under such conditions, the number of citrate-Au nanoparticles attached to the *A* features, although dictated by the surface area, needs to be arrived at empirically. On the basis of the number of particles per *A* feature, the surface coverage of citrate-Au nanoparticles equates to ~11%. If the *A* features can be rendered strongly positive, *e.g.*, by the selective growth of PVP brushes, deposition of amino thiol self-assembled monolayers, or use of polyelectrolyte

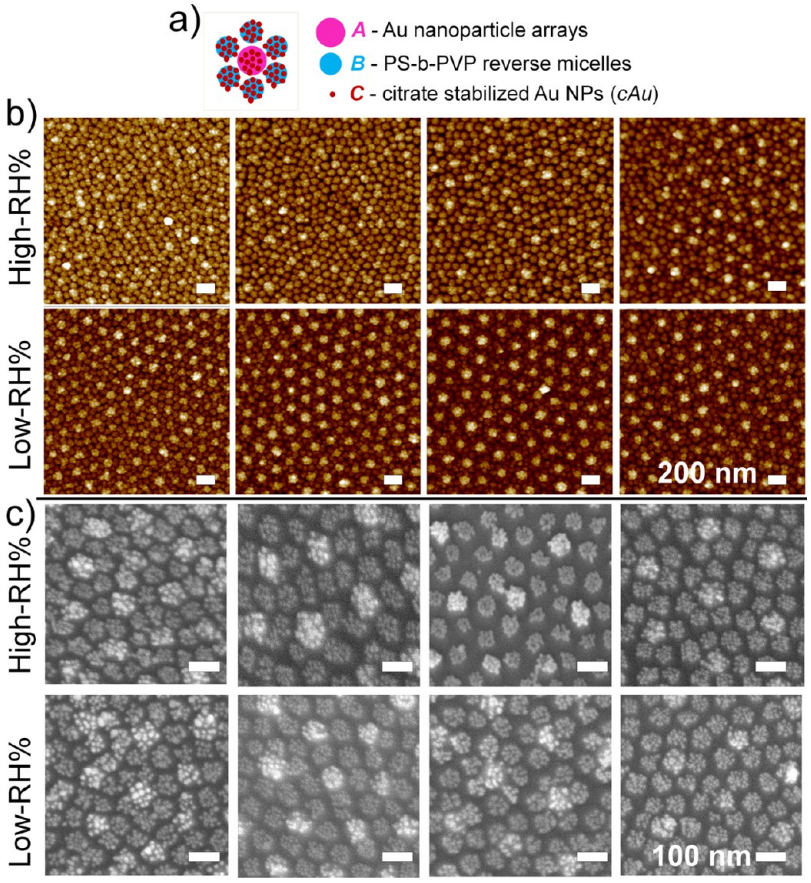

Figure 7. (a) Schematic illustration showing relative positions of the *A*, *B*, and *C* components within (*ACy*)(*BCz*)*x* ternary superstructures, followed by (b) tapping mode AFM (brighter pixels are taller; refer to Figure S10, SI, for measurements with z-scale information) and (c) FESEM images of $(Au \cdot cAu_y)$(PS-*b*-P2VP$\cdot cAu_z)_x$ at low and high RH% and increasing *x* from left to right.

multilayers, the density of citrate-Au features can be significantly increased close to the jamming limit of 54.7%.[54] The generality in the attainment of ternary superstructures is seen from the similar arrangement obtained even when TiO_2 nanoparticles were employed as the *A* features (Figure 8), thus precluding any chemical specificity of the process to Au as material. In addition, the polymeric template can be removed to yield superstructures consisting of entirely gold or semiconductor–gold combinations (Figure S9 in the SI for SEM images). In principle, a selectivity in the attachment of *C* features to either *A* or *B* features (thereby resulting in hierarchies with *y* or $z = 0$) can be achieved through appropriate surface functionalization of *A* or *B* in relation to *C* features employing established protocols in surface chemistry.

The approaches in this work can thus be seen as carrying fewer restrictions on the attainable material combinations by exploiting the options available at each step. The resulting arrays can pack high functional diversity per superstructure. We therefore envisage the utility of the assemblies in research areas that exploit interactions between nanostructures, *e.g.*, plasmon–plasmon, plasmon–exciton phenomena or placement

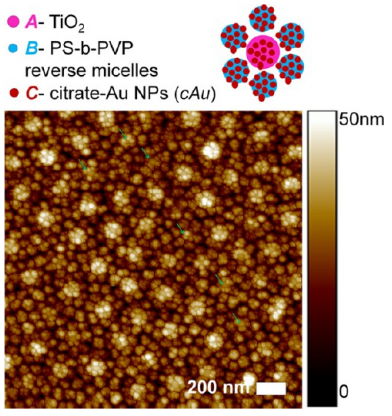

Figure 8. Tapping mode AFM image of $(TiO_2 \cdot cAu_y)$(PS-*b*-P2VP$\cdot cAu_z)_x$ superstructure arrays consisting of TiO_2 nanoparticle arrays (*A*) surrounded by PS-*b*-P2VP reverse micelles (*B*), with citrate-Au nanoparticles (*cAu*) (*C*) adsorbed onto *A* and *B* features (as illustrated in the schematic). The green arrows point to areas where the $TiO_2 \cdot cAu_y$ features do not show up prominently due to the smaller size of TiO_2 particles, representing a population at the tail end of the size distribution curve.

of biological receptors that require high control over the lateral resolutions and composition. The realization of the assemblies on macroscopic substrate areas will

enable probing such interactions using less demanding techniques with macroscopic analysis footprints. The stability of the assemblies especially toward adherence of the nanoparticles at each level of hierarchy is promising for the application of the bare assemblies. The binary and ternary assemblies that consist of the polymer template are stable in aqueous media even at high ionic strength and to temperatures until the glass transition temperature (T_g ~100 °C). The polymeric features change morphology (height, shape) upon exposure to solvents that swell the core or coronal blocks of the reverse micelles. This may be overcome upon cross-linking one or both of the blocks.[55,56] The assemblies where the polymers have been removed exhibit higher stability, as can be expected from the presence of purely inorganic materials. In any case, the assemblies are not resistant to mechanical scratches nor to ultrasonication, as can be expected for nanoparticulate films in general. For applications that do not require the use of bare assemblies, overlayer coatings of inorganic materials such as SiO_2 can be applied to significantly enhance thermal, mechanical, and chemical stability of the assemblies. The approaches in this work present the first layer of development that can be extended to adapt to a desired application, through suitable engineering and customization.

CONCLUSIONS

In summary, we have demonstrated an entirely self-assembly-driven hierarchical approach to fabricating binary and ternary superstructures exhibiting a high degree of flexibility in material type and composition. The approach takes advantage of the self-assembly of reverse micelles of block copolymers to produce arrays with a controlled periodicity (centre-to-centre distance), which enables fine-tuning the composition of the binary superstructures. Further advantage is drawn from the functionality of the core of the reverse micelles that allows both *in situ* synthesis of materials and directed electrostatic self-assembly of nanoparticles from the solution phase. The generic nature of the process used to create material nanostructures at each level of hierarchy allows significant flexibility in the choice of material types. This was demonstrated by the fabrication of superstructures consisting of Au, ZnO, TiO_2, and functional polymer nanostructures with different combinations. The approach is attractive for its simplicity and ease with which it can produce macroscopic arrays of superstructures, using processing that is quick to implement. The approach thus provides an excellent platform to realize multilevel hierarchy and multifunctionality, with control over the degree of hierarchy or functionality, respectively.

METHODS

Fabrication of *A* Arrays. The silicon substrates were diced and cleaned by ultrasonicating in acetone followed by 2-propanol and finally exposed to UV/ozone (UV-1, SAMCO Inc., Kyoto, Japan) for 10 min. Reverse micelles from a 0.5% (w/w) solution of the PS-*b*-PVP, 380 kDa, $f_{PS} \approx 0.5$, PDI 1.1, from *m*-xylene were spin-coated (CEE model 100CB spinner, Brewer Science Inc., MO, USA) at 1000, 2000, 4000, or 6000 rpm on Si substrates at high (RH ≈ 55%) or low humidity (RH < 10%). The reverse micelles in solutions were characterized using dynamic light scattering (90Plus particle size analyzer, Brookhaven Instruments Corporation, NY, USA). For controlling humidity during the spin-coating step, the spin-coater was placed within a custom-built chamber from Electro-Tech Systems, Inc. (ETS, PA, USA) that was designed to offer a closed-feedback humidity control in an operating range of 1−100% RH. For the preparation of *A* arrays consisting of gold features, the spin-coated substrates were immersed in an aqueous solution of 5 mg/mL of $HAuCl_4$ for 15 min, rinsed with deionized (DI) water, and blown dry using nitrogen. The polymer template was subsequently removed by O_2 plasma RIE (20 sccm O_2, 65 mTorr, 30 W for 15 min) to form Au nanoparticle arrays. *A* features consisting of TiO_2 nanoarrays were prepared by subjecting the reverse micelle arrays to $TiCl_4$ precursors within atomic layer deposition equipment, as reported elsewhere.[37] Briefly, $TiCl_4$ and H_2O were introduced into the atomic layer deposition chamber in pulses (100 cycles). N_2 gas was used as both a carrier gas and purge gas. The number of cycles precisely determines the amount of precursor impregnated into the hydrophilic PVP core. The polymer template was removed by subjecting it to O_2 plasma RIE to result in TiO_2 arrays. AFM (Nanoscope IV Multimode AFM, Veeco Instruments Inc., NY, USA) in the tapping mode and FESEM (JEOL 6700F, Tokyo, Japan) were used to characterize the nanopatterns during each step of fabrication.

Fabrication of *AB*x Arrays. The second level hierarchy was obtained by spin-coating reverse micelles of PS-*b*-P2VP (114 kDa, $f_{PS} \approx 0.5$) (*B*) onto pre-existing *A* arrays (with either Au or TiO_2 arrays) at 3000 rpm for 45 s to result in *Au*(PS-*b*-P2VP)$_x$ and *TiO*$_2$(PS-*b*-P2VP)$_x$ assemblies (Figure 6). *TiO*$_2$(*Au*)$_x$ were obtained by incubating *TiO*$_2$(PS-*b*-P2VP)$_x$ in an aqueous solution of 5 mg/mL $HAuCl_4$ for 15 min, rinsing with DI water, and blowing dry using nitrogen followed by an exposure to oxygen plasma RIE as before to remove the polymer. *Au*(*ZnO*)$_x$ arrays were prepared by incubating *Au*(PS-*b*-P2VP)$_x$ arrays in a solution of 1 M zinc chloride in water for 15 min, rinsing, and blowing dry using nitrogen, followed by exposure to oxygen plasma.

Fabrication of (*ACy*)(*BCz*)x Arrays. Ternary superstructure arrays of the type (*Au*·*cAu*$_y$)(PS-*b*-P2VP·*cAu*$_z$)$_x$ (Figure 7) with *A* = *Au*, *B* = PS-*b*-P2VP, *C* = citrate-Au nanoparticles (*cAu*) were obtained by immersing *Au*(PS-*b*-P2VP)$_x$ into a citrate-stabilized gold nanoparticle suspension for 2 h. Similarly, (*TiO*$_2$·*cAu*$_y$)(PS-*b*-P2VP·*cAu*$_z$)$_x$ (Figure 8) with *A* = TiO_2, *B* = PS-*b*-P2VP, and *C* = citrate-Au nanoparticles were obtained by incubating *TiO*$_2$-(PS-*b*-P2VP)$_x$ in a suspension of citrate-Au nanoparticles for a duration of 2 h. The citrate-stabilized colloidal Au nanoparticles were produced using the method described elsewhere.[57]

Estimation of Volume of the Solution Consisting of x_N Micelles. The hydrodynamic size (2 × *Rh*) of PS-*b*-P2VP 114 kDa, $f_{PS} \approx 0.5$ reverse micelles as measured using DLS was found to be 104 nm. From the R_g/R_h ratio values commonly encountered for spherical micelles of ~0.75,[38,58] R_g can be estimated to be ~39 nm. This can be taken as the dry-state radius of the micelle. From the volume of an equivalent sphere (of radius R_g) and assuming a density of 1.1 g/cm^3, the mass of a single micelle can be estimated to be 2.7×10^{-16} g. From the concentration of the polymer solution (0.005 g/mL), this would represent $\sim 1.8 \times 10^{13}$ micelles per cm^3 of the solution. This would equate to 1 micelle per 5.5×10^{-14} cm^3 (or 55 attoliters (aL)) of solution, based on which the volume of the solution containing 3−8

micelles (corresponding to the values of x_N in Figure 5) can be calculated to be ~164–437 aL. A minor deviation from this estimation is expected to arise based on the actual experimental value for R_g/R_h. Nevertheless, the estimation adequately serves to delineate the relative orders of magnitude for the volume of the micelle solution consisting of x_N micelles in relation to that of the Au features. The mean volume of the *A* features can be estimated by approximating them as hemispheres, as supported by height and diameter values measured by AFM and SEM. For the Au nanoparticles shown in Figure 5, the feature width varies between 68 and 122 nm, and their resulting volumes can be estimated to be ~0.09–0.48 aL.

Conflict of Interest: The authors declare no competing financial interest.

Acknowledgment. Funding support received from Joint Council Office (JCO) of the Agency for Science Technology and Research (A*STAR), through grant 10/3/EG/05/04, and from IMRE through grant IMRE/08-1C0314 is gratefully acknowledged. The authors appreciate Ren Bin (IMRE) for assistance with ALD of TiO_2, H. Y. Low (IMRE) Low (IMRE) for her support, and SnFPC, IMRE, for access to fabrication and characterization facilities. V.S. thanks National University of Singapore (NUS) for a grant of research scholarship.

Supporting Information Available: Additional information pertaining to geometric characterization of the assemblies, light scattering measurements, and calculation of geometric parameters is available free of charge *via* the Internet at http://pubs.acs.org.

REFERENCES AND NOTES

1. Feng, L.; Li, S.; Li, Y.; Li, H.; Zhang, L.; Zhai, J.; Song, Y.; Liu, B.; Jiang, L.; Zhu, D. Super-Hydrophobic Surfaces: From Natural to Artificial. *Adv. Mater.* **2002**, *14*, 1857–1860.
2. Weatherbee, S. D.; Nijhout, H. F.; Grunert, L. W.; Halder, G.; Galant, R.; Selegue, J.; Carroll, S. Ultrabithorax Function in Butterfly Wings and the Evolution of Insect Wing Patterns. *Curr. Biol.* **1999**, *9*, 109–115.
3. Stavenga, D. G.; Foletti, S.; Palasantzas, G.; Arikawa, K. Light on the Moth-Eye Corneal Nipple Array of Butterflies. *Proc. R. Soc. B* **2006**, *273*, 661.
4. Ikkala, O.; ten Brinke, G. Hierarchical Self-Assembly in Polymeric Complexes: Towards Functional Materials. *Chem. Commun.* **2004**, 2131–2137.
5. Park, J. W.; Thomas, E. L. Multiple Ordering Transitions: Hierarchical Self-Assembly of Rod-Coil Block Copolymers. *Adv. Mater.* **2003**, *15*, 585–587.
6. Krishnamoorthy, S.; van den Boogaart, M. A. F.; Brugger, J.; Hibert, C.; Pugin, R.; Hinderling, C.; Heinzelmann, H. Combining Micelle Self-Assembly with Nanostencil Lithography to Create Periodic/Aperiodic Micro-/Nanopatterns on Surfaces. *Adv. Mater.* **2008**, *20*, 3533–3538.
7. Zhang, F.; Low, H. Y. Ordered Three-Dimensional Hierarchical Nanostructures by Nanoimprint Lithography. *Nanotechnology* **2006**, *17*, 1884.
8. Alaeian, H.; Dionne, J. A. Plasmon Nanoparticle Superlattices as Optical-Frequency Magnetic Metamaterials. *Opt. Express* **2012**, *20*, 15781–15796.
9. Urban, J. J.; Talapin, D. V.; Shevchenko, E. V.; Kagan, C. R.; Murray, C. B. Synergism in Binary Nanocrystal Superlattices Leads to Enhanced P-Type Conductivity in Self-Assembled PbTe/Ag_2Te Thin Films. *Nat. Mater.* **2007**, *6*, 115–121.
10. Talapin, D. V. LEGO Materials. *ACS Nano* **2008**, *2*, 1097–1100.
11. Bao, N.; Gupta, A. Self-Assembly of Superparamagnetic Nanoparticles. *J. Mater. Res.* **2011**, *26*, 111–121.
12. Zeng, H.; Li, J.; Liu, J. P.; Wang, Z. L.; Sun, S. Exchange-Coupled Nanocomposite Magnets by Nanoparticle Self-Assembly. *Nature* **2002**, *420*, 395–398.
13. Nosonovsky, M.; Bhushan, B. Multiscale Effects and Capillary Interactions in Functional Biomimetic Surfaces for Energy Conversion and Green Engineering. *Philos. Trans. R. Soc., A* **2009**, *367*, 1511–1539.
14. Sotiropoulou, S.; Sierra-Sastre, Y.; Mark, S. S.; Batt, C. A. Biotemplated Nanostructured Materials. *Chem. Mater.* **2008**, *20*, 821–834.
15. Arnold, M.; Cavalcanti-Adam, E. A.; Glass, R.; Blummel, J.; Eck, W.; Kantlehner, M.; Kessler, H.; Spatz, J. P. Activation of Integrin Function by Nanopatterned Adhesive Interfaces. *ChemPhysChem* **2004**, *5*, 383–388.
16. Sun, Z.; Luo, Z.; Fang, J. Assembling Nonspherical 2D Binary Nanoparticle Superlattices by Opposite Electrical Charges: The Role of Coulomb Forces. *ACS Nano* **2010**, *4*, 1821–1828.
17. Chen, Z.; O'Brien, S. Structure Direction of II–VI Semiconductor Quantum Dot Binary Nanoparticle Superlattices by Tuning Radius Ratio. *ACS Nano* **2008**, *2*, 1219–1229.
18. Dong, A.; Chen, J.; Vora, P. M.; Kikkawa, J. M.; Murray, C. B. Binary Nanocrystal Superlattice Membranes Self-Assembled at the Liquid-Air Interface. *Nature* **2010**, *466*, 474–477.
19. Shevchenko, E. V.; Talapin, D. V.; Kotov, N. A.; O'Brien, S.; Murray, C. B. Structural Diversity in Binary Nanoparticle Superlattices. *Nature* **2006**, *439*, 55–59.
20. Kitaev, V.; Ozin, G. A. Self-Assembled Surface Patterns of Binary Colloidal Crystals. *Adv. Mater.* **2003**, *15*, 75–78.
21. Evers, W. H.; Friedrich, H.; Filion, L.; Dijkstra, M.; Vanmaekelbergh, D. Observation of a Ternary Nanocrystal Superlattice and Its Structural Characterization by Electron Tomography. *Angew. Chem., Int. Ed.* **2009**, *48*, 9655–9657.
22. Talapin, D. V.; Shevchenko, E. V.; Bodnarchuk, M. I.; Ye, X.; Chen, J.; Murray, C. B. Quasicrystalline Order in Self-Assembled Binary Nanoparticle Superlattices. *Nature* **2009**, *461*, 964–967.
23. Mukhopadhyay, R.; Al-Hanbali, O.; Pillai, S.; Hemmersam, A. G.; Meyer, R. L.; Hunter, A. C.; Rutt, K. J.; Besenbacher, F.; Moghimi, S. M.; Kingshott, P. Ordering of Binary Polymeric Nanoparticles on Hydrophobic Surfaces Assembled from Low Volume Fraction Dispersions. *J. Am. Chem. Soc.* **2007**, *129*, 13390–13391.
24. Lee, I.; Zheng, H.; Rubner, M. F.; Hammond, P. T. Controlled Cluster Size in Patterned Particle Arrays *via* Directed Adsorption on Confined Surfaces. *Adv. Mater.* **2002**, *14*, 572–577.
25. Qin, D.; Xia, Y.; Xu, B.; Yang, H.; Zhu, C.; Whitesides, G. M. Fabrication of Ordered Two-Dimensional Arrays of Micro- and Nanoparticles Using Patterned Self-Assembled Monolayers as Templates. *Adv. Mater.* **1999**, *11*, 1433–1437.
26. Yap, F. L.; Thoniyot, P.; Krishnan, S.; Krishnamoorthy, S. Nanoparticle Cluster Arrays for High-Performance SERS through Directed Self-Assembly on Flat Substrates and on Optical Fibers. *ACS Nano* **2012**, *6*, 2056–2070.
27. Lee, W.; Lee, S. Y.; Briber, R. M.; Rabin, O. Self-Assembled SERS Substrates with Tunable Surface Plasmon Resonances. *Adv. Funct. Mater.* **2011**, *21*, 3424–3429.
28. Kuemin, C.; Cathrein Huckstadt, K.; Lortscher, E.; Rey, A.; Decker, A.; Spencer, N. D.; Wolf, H. Selective Assembly of Sub-Micrometer Polymer Particles. *Adv. Mater.* **2010**, *22*, 2804–2808.
29. Wang, Y.; Chen, G.; Yang, M.; Silber, G.; Xing, S.; Tan, L. H.; Wang, F.; Feng, Y.; Liu, X.; Li, S. A Systems Approach towards the Stoichiometry-Controlled Hetero-Assembly of Nanoparticles. *Nat. Commun.* **2010**, *1*, 87.
30. Li, W.; Camargo, P. H.; Lu, X.; Xia, Y. Dimers of Silver Nanospheres: Facile Synthesis and Their Use As Hot Spots for Surface-Enhanced Raman Scattering. *Nano Lett.* **2008**, *9*, 485–490.
31. Chen, G.; Wang, Y.; Yang, M.; Xu, J.; Goh, S. J.; Pan, M.; Chen, H. Measuring Ensemble-Averaged Surface-Enhanced Raman Scattering in the Hotspots of Colloidal Nanoparticle Dimers and Trimers. *J. Am. Chem. Soc.* **2010**, *132*, 3644–3645.
32. Brousseau, L. C., III; Novak, J. P.; Marinakos, S. M.; Feldheim, D. L. Assembly of Phenylacetylene-Bridged Gold Nanocluster Dimers and Trimers. *Adv. Mater.* **1999**, *11*, 447–449.
33. Lee, J.; Wernette, D.; Yigit, M.; Liu, J.; Wang, Z.; Lu, Y. Site-Specific Control of Distances between Gold Nanoparticles Using Phosphorothioate Anchors on DNA and a Short Bifunctional Molecular Fastener. *Angew. Chem., Int. Ed.* **2007**, *46*, 9006–9010.
34. Nakata, K.; Hu, Y.; Uzun, O.; Bakr, O.; Stellacci, F. Chains of Superparamagnetic Nanoparticles. *Adv. Mater.* **2008**, *20*, 4294–4299.

35. Wustholz, K. L.; Henry, A. I.; McMahon, J. M.; Freeman, R. G.; Valley, N.; Piotti, M. E.; Natan, M. J.; Schatz, G. C.; Duyne, R. P. V. Structure−Activity Relationships in Gold Nanoparticle Dimers and Trimers for Surface-Enhanced Raman Spectroscopy. *J. Am. Chem. Soc.* **2010**, *132*, 10903–10910.
36. Spatz, J. P.; Mossmer, S.; Hartmann, C.; Moller, M.; Herzog, T.; Krieger, M.; Boyen, H. G.; Ziemann, P.; Kabius, B. Ordered Deposition of Inorganic Clusters from Micellar Block Copolymer Films. *Langmuir* **2000**, *16*, 407–415.
37. Krishnamoorthy, S.; Manipaddy, K. K.; Yap, F. L. Wafer-Level Self-Organized Copolymer Templates for Nanolithography with Sub-50 nm Feature and Spatial Resolutions. *Adv. Funct. Mater.* **2011**, *21*, 1102–1112.
38. Krishnamoorthy, S.; Pugin, R.; Brugger, J.; Heinzelmann, H.; Hinderling, C. Tuning the Dimensions and Periodicities of Nanostructures Starting from the Same Polystyrene-Block-Poly(2-Vinylpyridine) Diblock Copolymer. *Adv. Funct. Mater.* **2006**, *16*, 1469–1475.
39. Kastle, G.; Boyen, H. G.; Weigl, F.; Lengl, G.; Herzog, T.; Ziemann, P.; Riethmuller, S.; Mayer, O.; Hartmann, C.; Spatz, J. P.; *et al*. Micellar Nanoreactors - Preparation and Characterization of Hexagonally Ordered Arrays of Metallic Nanodots. *Adv. Funct. Mater.* **2003**, *13*, 853–861.
40. Hecht, U.; Schilz, C. M.; Stratmann, M. Influence of Relative Humidity during Film Formation Processes on the Structure of Ultrathin Polymeric Films. *Langmuir* **1998**, *14*, 6743–6748.
41. Kuo, Y. K.; Chao, C. G. Control Ability of Spin Coating Planarization of Resist Filmand Optimal Control of Developers. *Microelectron. J.* **2006**, *37*, 759–764.
42. Vogt, B. D.; Christopher, L.; Jones, R. L.; Wang, C. Y.; Lin, E. K.; Wu, W.; Satija, S. K.; Goldfarb, D. L.; Angelopoulos, M. Interfacial Effects on Moisture Absorption in Thin Polymer Films. *Langmuir* **2004**, *20*, 5285–5290.
43. Tan, K. T.; Vogt, B. D.; White, C. C.; Steffens, K. L.; Goldman, J.; Satija, S. K.; Clerici, C.; Hunston, D. L. On the Origins of Sudden Adhesion Loss at a Critical Relative Humidity: Examination of Bulk and Interfacial Contributions. *Langmuir* **2008**, *24*, 9189–9193.
44. Piner, R. D.; Mirkin, C. A. Effect of Water on Lateral Force Microscopy in Air. *Langmuir* **1997**, *13*, 6864–6868.
45. Yada, T.; Maejima, T.; Aoki, M. Formation of a Positive Photoresist Thin Film by Spin Coating: Influence of Atmospheric Humidity. *Jpn. J. Appl. Phys.* **1997**, *36*, 7041–7047.
46. Roy, S.; Ansari, K. J.; Jampa, S. S. K.; Vutukuri, P.; Mukherjee, R. Influence of Substrate Wettability on the Morphology of Thin Polymer Films Spin-Coated on Topographically Patterned Substrates. *ACS Appl. Mater. Interfaces* **2012**, *4*, 1887–1896.
47. Rozhok, S.; Piner, R.; Mirkin, C. A. Dip-Pen Nanolithography: What Controls Ink Transport? *J. Phys. Chem. B* **2003**, *107*, 751–757.
48. Riedo, E.; Levy, F.; Brune, H. Kinetics of Capillary Condensation in Nanoscopic Sliding Friction. *Phys. Rev. Lett.* **2002**, *88*, 185505.
49. Lange, N. A.; Dean, J. A. *Handbook of Chemistry*; McGraw-Hill: USA, 1934; p, 10.
50. Denkov, N. D.; Velev, O. D.; Kralchevsky, P. A.; Ivanov, I. B.; Yoshimura, H.; Nagayama, K. Two-Dimensional Crystallization. *Nature* **1993**, *361*, 26.
51. Lawrence, C. J. The Mechanics of Spin Coating of Polymer Films. *Phys. Fluids* **1988**, *31*, 2786–2795.
52. Haas, D. E.; Quijada, J. N.; Picone, S. J.; Birnie, D. P. Effect of Solvent Evaporation Rate on Skin Formation during Spin Coating of Complex Solutions. *Proc. SPIE* **2000**, *3943*, 280–284.
53. Hadjichristidis, N.; Pispas, S.; Floudas, G. Adsorption of Block Copolymers at Solid-Liquid Interfaces. In *Block Copolymers: Synthetic Strategies, Physical Properties, and Applications*; Wiley-Interscience, 2002; pp 232−254.
54. Oberholzer, M. R.; Stankovich, J. M.; Carnie, S. L.; Chan, D. Y. C.; Lenhoff, A. M. 2-D and 3-D Interactions in Random Sequential Adsorption of Charged Particles. *J. Colloid Interface Sci.* **1997**, *194*, 138–153.
55. Hayward, R. C.; Chmelka, B. F.; Kramer, E. J. Crosslinked Poly(Styrene)-Block-Poly(2-Vinylpyridine) Thin Films as Swellable Templates for Mesostructured Silica and Titania. *Adv. Mater.* **2005**, *17*, 2591–2595.
56. Zhang, R.; Cherdhirankorn, T.; Graf, K.; Koynov, K.; Berger, R. Swelling of Cross-Linked Polystyrene Beads in Toluene. *Microelectron. Eng.* **2008**, *85*, 1261–1264.
57. Grabar, K. C.; Griffith Freeman, R.; Hommer, M. B.; Natan, M. J. Preparation and Characterization of Au Colloid Monolayers. *Anal. Chem.* **1995**, *67*, 735–743.
58. Helmstedt, M.; Schafer, H. Determination of Sizes of Spherical Particles, Prepared by Dispersion Polymerization of Methyl Methacrylate in Non-Aqueous Medium, by Analysis of the Particle Scattering and Autocorrelation Functions. *Polymer* **1994**, *35*, 3377–3383.